JOURNAL OF SPACECRAFT AND ROCKETS
Vol. 36, No. 4, July–August 1999

Simple Analytical Model for Parametric Studies of Hypersonic Waveriders

Ryan P. Starkey* and Mark J. Lewis†
University of Maryland, College Park, Maryland 20742

An analytical, power-law-derived hypersonic waverider model is developed using a three-dimensional wedge-based flowfield with viscous effects. The model is designed for simple parametric tradeoffs and understanding of more complex optimization results. This analytical model is validated against a viscous optimized conical waverider created using an inverse design technique. Off-design performance of the analytical model at varying Mach numbers and angles of attack is validated using an optimized shock-defined waverider (which itself has been validated with a computational Euler calculation). Both the variable-wedge-angle waverider and shock-defined waverider calculations had the same magnitude of error in comparison to the lift-to-drag ratios of the computational Euler validation of the shock-defined waverider (maximum of 2% difference). The variable-wedge-angle method is shown to calculate the same aerodynamic and geometric properties of higher-order methods in orders of magnitude less time.

Nomenclature

A, B, C	= power law scaling parameters
D	= drag, N
F	= hypergeometric function
G	= flight condition function
h	= height, m
L	= lift, N
ℓ	= length, m
M	= Mach number
m, n	= power law exponents
P	= pressure, Pa
R	= thermodynamic constant, KJ/(kg K)
S	= area, m^2
T	= temperature, K
U	= velocity magnitude, m/s
V	= volume, m^3
w	= width, m
X, Y	= L/D functions
x, y, z	= linear dimensions, m
α	= angle of attack, deg
β	= oblique shock inclination angle, deg
δ	= leading-edge inclination angle, deg
η	= volumetric efficiency
θ	= vehicle centerline wedge angle, deg
μ	= viscosity, Ns/m^2
ξ	= streamline length, m
ρ	= density, kg/m^3
σ	= angle-of-attack constant
τ	= shear stress, N/m^2
ϕ	= local wedge angle
Ψ	= L/D functions

Subscripts

alt	= altitude
av	= average
b	= value for base surface
c	= value for compression surface, caretlike
cc	= concave
cv	= convex
e	= property at edge of boundary layer
l	= value for lower surface
lam	= laminar
nc	= noncaretlike
p	= planform
s	= surface area of a sphere
turb	= turbulent
u	= value for upper surface
V_s	= based on volume of a sphere
v	= viscous
w	= wall value, wetted surface area, wave drag
∞	= freestream value or surface

Received 14 April 1998; revision received 10 November 1998; accepted for publication 10 November 1998.

*Graduate Research Assistant, Department of Aerospace Engineering; rstarkey@eng.umd.edu. Student Member AIAA.

†Associate Professor, Department of Aerospace Engineering. Associate Fellow AIAA.

Introduction

A PROMISING concept for the design of high lift-to-drag (L/D) hypersonic vehicles is the waverider, presented by Nonweiler[1] in 1959. Waveriders are designed so that the bow shock is attached everywhere to the sharp leading edge. As a result of this attached shock, waveriders exhibit very high values of L/D, as shown by theory,[2] experiment,[3] and computation,[4] although not necessarily the lowest drag. The high lift generated by waveriders is provided by a region of high-pressure air, which exists between the under surface and the attached shock.

This paper will explore the aspects of parametric design of hypersonic waveriders using a wedge-derived, power-law-shaped vehicle with either constant or variable spanwise wedge angles. An advantage to these models is their versatility in generating a wide variety of geometries, which closely mimic inverse hypersonic vehicle designs, while still retaining the analytical calculation simplicity of the more generic caret waveriders, generated from a simple wedge flowfield.

Modeling of Vehicles with Two-Dimensional Shocks

Geometry

A general description of waverider geometries is derived with two-dimensional power law equations that define the curvature of both the planform p and upper u surfaces:

$$y_p = Ax^n \tag{1}$$

$$y_u = B(z_u)^n \rightarrow z_u = (y_u/B)^{1/n} \tag{2}$$

where the zero coordinate point is at the nose centerline with the height defined as positive going down, as shown in Fig. 1. Parameters A and B are positive sizing constants, and exponent n can vary within the range $0 \rightarrow 1$.

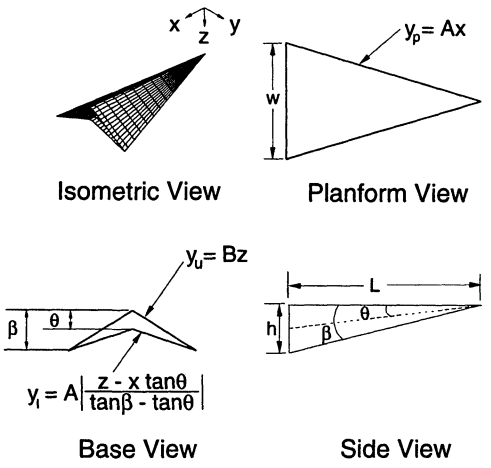

Fig. 1 Caret-waverider example: $A = 0.3$, $n = 1.0$, $\theta = 5$ deg, and $\ell = 50$ m.

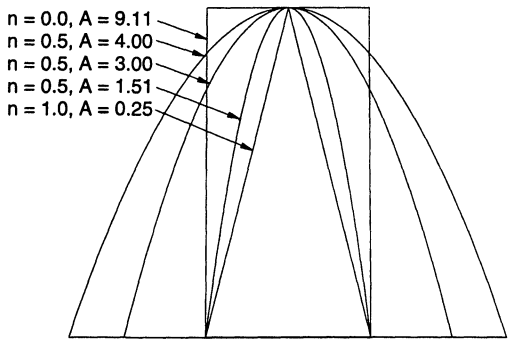

Fig. 2 Variations in power law constant A and exponent n (planform view).

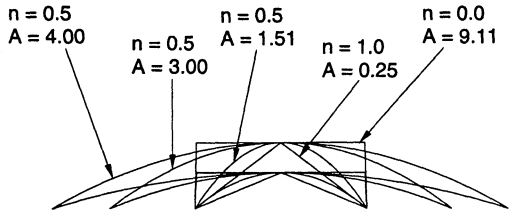

Fig. 3 Variations in power law constant A and exponent n (base view).

To ensure a planar shock, i.e., a wedge-derived flowfield, the vehicle must have a constant wedge angle θ. A planar shock is guaranteed by constraining the curvature of the lower surface to follow the equation

$$\tan\theta = \frac{z_l - (y_u/B)^{1/n}}{x - (y_p/A)^{1/n}} \tag{3}$$

Applying Eq. (1) between $x = 0$ and the desired vehicle length $x = \ell$ along with Eq. (2) defines the entire vehicle upper surface. Similarly, applying Eq. (1) between $x = 0$ and the lower surface length, $x = \ell/\cos\theta$, along with Eq. (3) defines the vehicle lower surface. The vehicle base plane is taken perpendicular to the flight path at a 0-deg angle of attack. These equations result in five variables (A, B, n, ℓ, and θ) that may be manipulated to generate a wide variety of vehicle configurations.

Small variations of these five parameters can result in large variations in the resulting vehicle geometry, as shown in Figs. 2 and 3. At a value of $n = 0$, the vehicle takes on a blunt-planform (spatulate) flat-topped configuration, whereas at $n = 1$ the vehicle is a caret geometry.

Waveriders are designed assuming an attached leading-edge shock. Not all variable combinations possible with this parametric geometry will lead to a valid waverider with an attached shock. Shock attachment is determined by setting

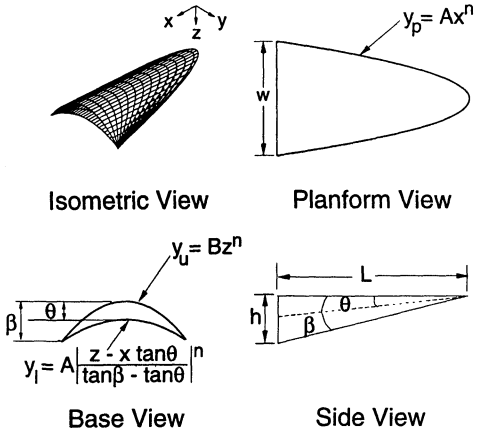

Fig. 4 Constant-wedge-angle waverider example: $A = 0.66$, $n = 0.5$, $\theta = 5$ deg, and $\ell = 50$ m.

$$B = \frac{A}{\tan^n\beta} \tag{4}$$

Substituting Eq. (4) into Eq. (3) results in

$$z_l = x\tan\theta + (y/A)^{1/n}(\tan\beta - \tan\theta) \tag{5}$$

for the curvature of the lower surface with an attached shock, where β must be less than the maximum shock attachment angle. An example of a vehicle generated using these equations is shown in Fig. 4. The attached shock requirement reduces the number of variable parameters to four: A, n, ℓ, and θ. This results in what has been termed the constant wedge angle method.

This power law vehicle model is simplistic enough to allow all geometric values to be defined analytically, allowing for quick analysis of different vehicles. The vehicle height h and width w are given by

$$h = (A/B)^{1/n}\ell = \ell\tan\beta \tag{6}$$

$$w = 2A\ell^n \tag{7}$$

Using Eq. (7), the variable parameters can be changed to a more convenient set consisting of ℓ, w, n, and θ.

The planform area S_p of the vehicle is found by integrating the area under the projected leading-edge curve, as viewed from above, resulting in

$$S_p = 2\int_0^\ell Ax^n = \frac{w\ell}{n+1} \tag{8}$$

As expected, the planform area of the spatulate vehicle ($n = 0$) is twice that of the caret vehicle ($n = 1$) for constant length and width.

Base area S_b is found from

$$S_b = 2\int_0^{A\ell^n}\int_{z_u}^{z_l} dz\,dy = S_p\tan\theta \tag{9}$$

Holding the values of w, ℓ, and θ constant and testing n at the two limiting values show that the spatulate vehicle ($n = 0$) will have twice the base area of the caret vehicle ($n = 1$).

The volume V for the wedge-derived, power-law waverider is

$$V = 2\int_0^\ell S_b(x)\,dx = \frac{S_b\ell}{n+2} = \frac{w\ell^2\tan\theta}{(n+1)(n+2)} \tag{10}$$

which is more sensitive to changes in the length than the width or wedge angle. Also, the denominator can vary between two (for $n = 0$) and six (for $n = 1$), with the $n = 0$ vehicle having three times the volume of the $n = 1$ vehicle with equal ℓ, w, and θ.

This parametric vehicle allows for many variations in possible configurations by simply changing the value of the power law exponent n. Also, all of the geometric equations listed reduce to the well-known caret waverider equations[2] at $n = 1$.

The freestream and compression wetted surface areas $S_{w\infty}$ and S_{wc}, respectively, are

$$S_{w\infty} = 2\int_0^{\ell}\int_0^{x\tan\beta}\sqrt{1+\frac{A^2n^2z^{2n-2}}{\tan^n\beta}}\,dz\,dx \tag{11}$$

$$S_{wc} = 2\int_0^{\ell}\int_{x\tan\theta}^{x\tan\beta}\sqrt{1+\frac{A^2n^2(z-x\tan\theta)^{2n-2}}{(\tan\beta-\tan\theta)^{2n}}}\,dz\,dx \tag{12}$$

The total wetted surface area of the vehicle is $S_w = S_{w\infty} + S_{wc}$. These may have to be integrated numerically. Alternatively, the summation of the cross products in the vehicle coordinate space provides a fast surface area calculation method.

The volume, wetted surface area, and planform area can then be used to calculate figures of merit, such as the volumetric efficiencies based on wetted surface area η_{S_w} or planform area η_{S_p}, defined as

$$\eta_{S_w} \equiv V^{\frac{2}{3}}/S_w \tag{13}$$

$$\eta_{S_p} \equiv V^{\frac{2}{3}}/S_p \tag{14}$$

Substituting Eqs. (8) and (10) into Eq. (14) results in

$$\eta_{S_p} \equiv \frac{V^{\frac{2}{3}}}{S_p} = \left[\frac{(n+1)}{(n+2)^2}\frac{\ell\tan^2\theta}{w}\right]^{\frac{1}{3}} \tag{15}$$

This shows the small variation in η_{S_p} achievable at the power law exponent limits of $n = 0$ (spatulate) and $n = 1$ (caret) for constant length, width, and wedge angle to be $\eta_{S_p,n=0} = 1.04\eta_{S_p,n=1}$. Therefore, even though the spatulate configuration has three times the volume of the caret configuration, it comes at the expense of added planform area and scales by about the same margin. For a true gain in η_{S_p}, the vehicle should gain all of its volume through height variations, i.e., by increasing θ, and by increasing the length-to-width ratio. The most efficient exponent n can be found by taking the derivative of η_{S_p} with respect to n and holding ℓ, w, and θ constant. This differentiation of η_{S_p} results in $n = 0$ as the exponent, which allows for the highest planform efficiency, i.e., spatulate configuration.

Nonconventional figures of merit have been developed to compare the vehicle against the properties of a sphere because a sphere is the most volumetrically efficient shape possible. Alternate volumetric efficiencies can be based on a comparison to a sphere of equal volume (surface area comparison) η_{S_s} or a sphere of equal surface area (volume comparison) η_{V_s}:

$$\eta_{S_s} \equiv \frac{(36\pi)^{\frac{1}{3}}V^{\frac{2}{3}}}{S_w} \tag{16}$$

$$\eta_{V_s} \equiv \frac{6\pi^{\frac{1}{2}}V}{S_w^{\frac{3}{2}}} \tag{17}$$

Aerodynamic Performance

Lift and Wave Drag

The flow over the waverider is assumed to be essentially two dimensional with streamlines flowing straight back over a series of wedges. Lift L and wave drag D_w are

$$L = S_b\sin|\alpha|(-1)^{\sigma}[P_b - P_l] + S_p\cos|\alpha|[P_l - P_u] \tag{18}$$

$$D_w = S_b\cos|\alpha|[P_l - P_b] + S_p\sin|\alpha|(-1)^{\sigma}[P_l - P_u] \tag{19}$$

where P_u, P_l, and P_b indicate the pressure for the upper, lower, and base surfaces, respectively, found using either oblique shock theory or Prantyl–Meyer expansion theory. The parameter $\sigma \equiv 1$ for negative angle of attack α and $\sigma \equiv 0$ for $\alpha \geq 0$.

Table 1 Viscous drag parameters and constants

Function	Laminar flow	Turbulent flow
G_1	$0.664\sqrt{\rho_e^2U_e^3\mu^*C^*/\rho^*}$	$0.037(U_e)^{1.8}(\rho^*)^{0.8}(\mu^*)^{0.2}$
G_2	0.5	0.8
F_0	0.99845	0.99758
F_1	−0.57529	−0.80941
F_2	0.36737	0.54989
F_3	−0.11939	−0.18247

Viscous Drag

Both the laminar and turbulent solutions have been derived using the reference temperature method.[5] In most cases, the transition point will be unknown, and so these two results will bracket the actual value. Following the two-dimensional streamline assumption, the viscous drag is estimated by integrating along two-dimensional streamlines over the area of the vehicle.

The skin friction for laminar flow $\tau_{w,\text{lam}}$ is

$$\tau_{w,\text{lam}} \approx 0.332\rho_eU_e^2\sqrt{\frac{C^*}{Re_x^*}} \equiv \frac{G_{1,\text{lam}}}{2x^{1-G_{2,\text{lam}}}} \tag{20}$$

where the conditions at the edge of the boundary layer are approximated using postshock conditions. Function $G_{1,\text{lam}}$ and $G_{2,\text{lam}}$ [defined in Eq. (20)] are shown in Table 1, where

$$Re^* = \frac{\rho^*U_ex}{\mu^*} \tag{21}$$

$$\rho^* = P/RT^* \tag{22}$$

The parameter C^* is the Chapman–Rubensin parameter evaluated at average boundary-layer conditions[5] and is solved for using the power law approximation given by

$$C^* = (T^*/T_e)^{n-1} \approx (T^*/T_e)^{-\frac{1}{3}} \tag{23}$$

for air, where T^*/T_e is found using Eckert's empirical estimate for the average boundary-layer temperature

$$T^*/T_e \approx 0.5 + 0.039M_e^2 + 0.5(T_w/T_e) \tag{24}$$

and the wall temperature is estimated depending on the application. To keep this model simple and analytical, a single estimate for the wall temperature is used over the entire vehicle. For hypersonic vehicles at cruise conditions, a reasonable estimate is $T_w \approx 1200$ K.

Dynamic viscosity at the reference temperature μ^* is approximated by Sutherland's law[5]:

$$\mu^*/\mu_r = (T^*/T_r)^{\frac{3}{2}}[(T_r + S)/(T^* + S)] \tag{25}$$

where S is a characteristic temperature for a particular gas (110 K for air). The reference value of viscosity μ_r and the reference temperature T_r are 1.79×10^{-5} kg/(ms) and 293.15 K, respectively, for air.

Laminar viscous drag D_{lam} is then found by integrating the skin friction over the length of a streamline $\xi(y)$ and then over all streamlines for the upper u and lower l surfaces, respectively:

$$D_{\text{lam},u} = G_{1,\text{lam},u}\int_0^{A\ell^n}\int_0^{\xi_u(y)}\frac{dx\,dy}{x^{\frac{1}{2}}} \tag{26}$$

$$D_{\text{lam},l} = G_{1,\text{lam},l}\int_0^{A\ell^n}\int_0^{\xi_u(y)/\cos\theta}\frac{dx\,dy}{x^{\frac{1}{2}}} \tag{27}$$

where $\xi_u(y)$ is the spanwise-dependent streamline length over the upper surface given by

$$\xi_u(y) = \ell[1 - (2y/w)^{1/n}] \tag{28}$$

The skin friction for high-speed turbulent plate flow[5] $\tau_{w,\text{turb}}$ is well approximated by

$$\tau_{w,\text{turb}} \approx \frac{0.0592\rho^* U_e^2}{2(Re^*)^{0.2}} = \frac{0.8\, G_{1,\text{turb}}}{x^{1-G_{2,\text{turb}}}} \tag{29}$$

where the functions $G_{1,\text{turb}}$ and $G_{2,\text{turb}}$ [defined in Eq. (29)] are shown in Table 1. Turbulent viscous drag D_{turb} is found by integrating Eq. (29) in the same manner as for the upper and lower surfaces:

$$D_{\text{turb},u} = 1.6 G_{1,\text{turb},u} \int_0^{A\ell^n} \int_0^{\xi_u(y)} \frac{1}{x^{0.2}}\, dx\, dy \tag{30}$$

$$D_{\text{turb},l} = 1.6 G_{1,\text{turb},l} \int_0^{A\ell^n} \int_0^{\xi_u(y)/\cos\theta} \frac{1}{x^{0.2}}\, dx\, dy \tag{31}$$

Because both the laminar and turbulent viscous drag equations are of the same form, they are evaluated in the same manner. The only difference between the equations for the upper and lower surfaces are the integration limits, i.e., $\xi_l(y) = \xi_u(y)/\cos\theta$. Therefore, the same equation can be used for the upper and lower surface because the upper surface is aligned with the freestream flow direction, i.e., using $\theta = 0$ deg, when evaluated with the proper atmospheric conditions. Integrating by parts in both the x and y directions results in a series solution for the viscous drag D_v, represented by a hypergeometric function of the form

$$D_v = \frac{G_1 w \ell^{G_2}}{(\cos\theta)^{G_2}} \left[\sum_{k=0}^{\infty} \frac{(n)_k (-G_2)_k}{(1+n)_k} \frac{1^k}{k!} \right] \tag{32}$$

The hypergeometric function can be rewritten as

$$\sum_{k=0}^{\infty} \frac{(n)_k (-G_2)_k}{(1+n)_k} \frac{1^k}{k!} = \sum_{k=0}^{\infty} \frac{1}{k!} \prod_{p=0}^{k} \frac{(n+p)(p-0.5)}{1+n+p} \tag{33}$$

which fits well to a third-order polynomial of the form

$$F(n) \equiv F_0 + F_1 n + F_2 n^2 + F_3 n^3 \tag{34}$$

for both the laminar and turbulent curves, where F_0, F_1, F_2, and F_3 are constants. This results in the combined laminar and turbulent drag equation for either the upper or lower surface of the vehicle

$$D_v = G_1 w F(n) (\ell/\cos\theta)^{G_2} \tag{35}$$

with the constants and functions, F and G, as shown in Table 1. It is easy to see that Eq. (35) scales linearly with the width and to the G_2 power of length. Also, the power law exponent n only appears within the function $F(n)$. Only the implicit functional dependence on θ cannot be readily determined due to the atmospheric properties in the variable G_1.

The plot of the hypergeometric function for both the laminar and turbulent cases is shown in Fig. 5 for variations in the power law exponent n from zero to one. Equation (35) shows that for a constant set of values for ℓ, w, and θ, the viscous drag scales by the hypergeometric function. For the laminar case, the viscous drag at $n = 1$ is 67% of the value at $n = 0$. Similarly, at $n = 1$ the turbulent drag is 56% of the $n = 0$ case. Therefore, even though the $n = 1$ vehicle has 33% of the volume and 50% of the planform area of the $n = 0$ vehicle, it has a disproportionately higher amount of viscous drag.

L/D Equation

The lift-to-drag ratio can be derived from the earlier defined L and D. Writing Eqs. (18), (19), and (35) in the form of the complete L/D equation

$$\frac{L}{D} = \frac{L}{D_w + D_v} \tag{36}$$

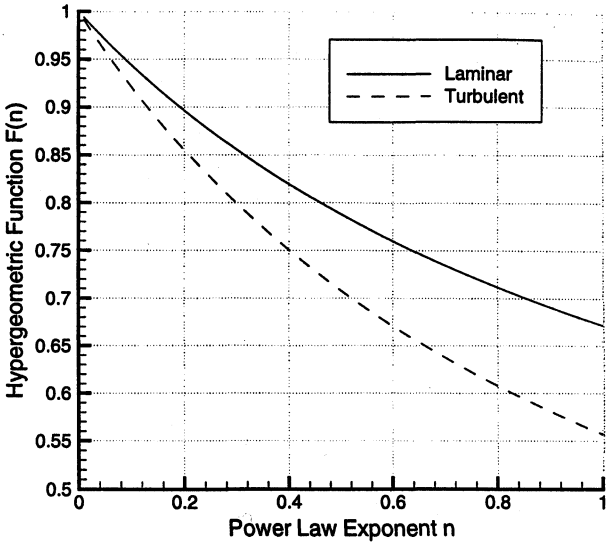

Fig. 5 Hypergeometric function $F(n)$ vs power law exponent n for fully laminar and turbulent cases.

and then dividing through by $\cos|\alpha|[P_l - P_u]$ and substituting Eq. (9) into S_b result in the following simplified L/D equation:

$$\frac{L}{D} = \frac{1}{\Psi_1(\theta, \alpha, M_\infty, h_{\text{alt}}) + \Psi_2(\theta, \alpha, M_\infty, h_{\text{alt}})\Psi_3(\ell)\Psi_4(n)} \tag{37}$$

where h_{alt} is the design or cruise altitude and

$$\Psi_1 \equiv (X + Y)/(1 - XY) \tag{38}$$

$$\Psi_2 \equiv \left[G_{1,u} + \frac{G_{1,l}}{(\cos\theta)^{G_2}} \right] \frac{1}{(P_l - P_u)\cos|\alpha|(1 - XY)} \tag{39}$$

$$\Psi_3 \equiv \ell^{\,G_2 - 1} \tag{40}$$

$$\Psi_4 \equiv (n+1)\left(F_0 + F_1 n + F_2 n^2 + F_3 n^3\right) \tag{41}$$

$$X \equiv \tan\theta \left[\frac{P_l - P_b}{P_l - P_u} \right] \tag{42}$$

$$Y \equiv (-1)^{\sigma} \tan|\alpha| \tag{43}$$

For a given design point Mach number and altitude, the L/D becomes a function of only θ, α, ℓ, and the power law exponent n. The smaller the denominator in Eq. (37), the larger the L/D becomes. Upon further investigation, it can be seen that the function Ψ_1 is like a wave drag or blockage term and $\Psi_2\Psi_3\Psi_4$ is like a viscous term. Both of these terms contain some component of lift of the vehicle through the function X, as well as the $(P_l - P_u)$ term in Ψ_2.

At $\alpha \approx -\theta/2$, the pressure term $(P_l - P_u)$ in the denominator of Ψ_2 and X goes to zero, but L/D is still defined. Taking the limit as $\alpha \to -\theta/2$, it can be found that Eq. (37) reduces to

$$\lim_{\alpha \to -\theta/2} \frac{L}{D} = -1 \Bigg/ \left\{ \frac{1}{Y} + \left[G_{1,u} + \frac{G_{1,l}}{(\cos\theta)^{G_2}} \right] \frac{\Psi_3(\ell)\Psi_4(n)}{(P_l - P_b) Y \tan\theta \cos|\alpha|} \right\} \tag{44}$$

Note that Eqs. (37) and (44) are independent of the width of the vehicle. This is an inherent characteristic due to the uniform wedge angle of the vehicle and, therefore, the constant flow properties along each streamline. Also, because the width scales with the constant A for a given exponent n, i.e., $w = 2A\ell^n$, the width of each streamline scales by the same constant, thereby scaling the viscous drag linearly in A. Using variations in the vehicle's width, the vehicle can be tailored to achieve any desired volume. This allows for incredible flexibility in choosing the design geometry.

Modeling of Vehicles with Three-Dimensional Shocks

Vehicle Geometry

The derived model can be expanded to include nonplanar (three-dimensional) shocks using what has been termed the variable-wedge-angle method. The methodology for the generation of this vehicle is the same as the constant-wedge-angle vehicle, with the addition of a third power law function to include lower surface curvature

$$y_{l,cc} = C(z_{l,cc} - x\tan\theta)^m \rightarrow z_{l,cc} = (y_{l,cc}/C)^{1/m} + x\tan\theta \quad (45)$$

for $\theta < \delta$, i.e., concave surface, where δ is the angle of the leading edge measured relative to freestream; m is a second power-law exponent, which can vary between 0 and 1; and C is the lower surface power law constant. A vehicle with a convex lower surface has curvature defined by

$$y_{l,cv} = C(-z_{l,cv} + x\tan\theta)^m \rightarrow z_{l,cv} = x\tan\theta - (y_{l,cv}/C)^{1/m} \quad (46)$$

Unlike the planar-shock vehicle, these equations result in six variables (n, m, w, ℓ, θ, and δ), which may be manipulated to generate a wide variety of vehicle designs where the upper surface power law constant is defined as $B = A/\tan^n\delta$. This is very similar to Eq. (4), where the shock angle β has been replaced by the leading-edge angle δ. The introduction of the parameter δ allows for the leading-edge angle to be defined independent of the shock angle (which is not constant for this geometry). The parameter C is a scaling factor used to align the leading edges of the upper and lower surfaces

$$C = \frac{Ax^{n-m}}{|\tan\theta - \tan\delta|^m} \quad (47)$$

Absolute value is used because C must always be positive, regardless of whether vehicle is convex or concave. The resulting equation for the lower surface (either convex or concave) is given by

$$z_l = x\tan\theta + \left(\frac{2y\ell^n}{wx^{n-m}}\right)^{1/m}(\tan\theta - \tan\delta) \quad (48)$$

An example of a convex vehicle generated using these equations is shown in Fig. 6.

This model can be reduced to a constant-wedge-angle vehicle with a three-dimensional shock for the cases with $n = m$ or to a constant-wedge-angle vehicle with a planar shock for the cases of $n = m$ and $\delta = \beta$. For $n = m = 1$ and $\delta = \beta$, these equations further reduce to the caret-style waverider. This model decomposition is shown in Table 2.

The lower surface cannot cross the upper surface, and so the ratio of the slopes at the leading edge

$$\frac{y'_{l,cc}}{y'_{u,cc}} = \frac{m}{n}\frac{\tan\delta}{\tan\delta - \tan\theta} \quad (49)$$

must be less than unity for the concave vehicle. An example of a shape in which this is not true is shown in Fig. 7. This can be

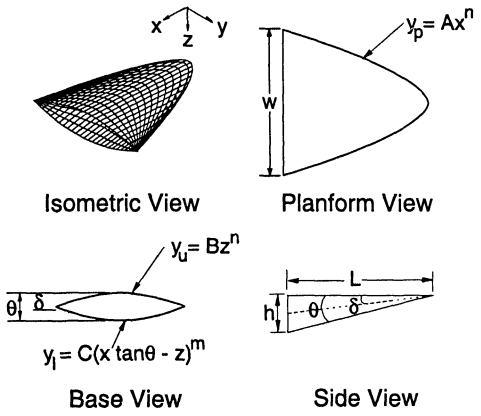

Fig. 6 Variable-wedge-angle convex waverider example: A = 2.1, m = 0.5, n = 0.6, θ =12 deg, δ = 6 deg, and ℓ =36.58 m.

Table 2 Variable wedge angle model decomposition

Shock	ϕ_{local}	Simplifications	Free variables
Three dimensional	Variable	N/A	$w, \ell, n, m, \theta, \delta$
Three dimensional	Constant	$m = n$	$w, \ell, n, \theta, \delta$
Two dimensional	Constant	$m = n, \delta = \beta$	w, ℓ, n, θ
Two dimensional caret	Constant	$m = n = 1, \delta = \beta$	w, ℓ, θ

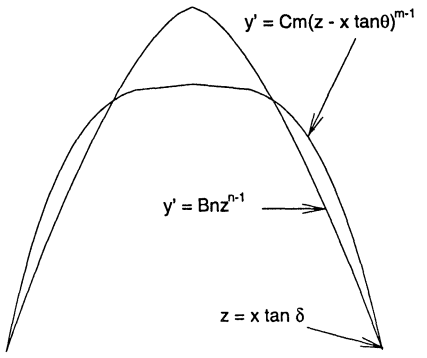

Fig. 7 Example of a nonphysical combination of variables (base view).

rewritten in terms of the following inequality for vehicles with an attached shock:

$$\frac{m}{n}\frac{\tan\delta}{\tan\delta - \tan\theta} > 1 \quad (50)$$

which must be satisfied for a feasible design.

Another way to write Eq. (49) is in terms of the minimum wedge angle for a given set of variables:

$$\theta_{cc,min} = \tan^{-1}\{\tan\delta[1 - (m/n)]\} \quad (51)$$

Height h, width w, and planform area S_p for the variable wedge angle vehicles are the same as shown in Eqs. (6–8) for the constant-wedge-angle vehicles. Base area S_b of the variable-wedge-angle vehicles can be found by solving the equations

$$S_b = 2\int_0^{w/2}\int_{z_u}^{z_l} dz\,dy \quad (52)$$

where the z coordinate of the upper surface is found from Eq. (2) and the z coordinates for the lower surfaces of either the concave or convex geometries are found from Eq. (48). The solution has been divided into two terms, $S_{b,c}$ and $S_{b,nc}$, shown by the equations

$$S_{b,c} = S_p\tan\theta[(n+1)/(m+1)] \quad (53)$$

$$S_{b,nc} = S_p\tan\delta[(m-n)/(m+1)] \quad (54)$$

where $S_b = S_{b,c} + S_{b,nc}$. Equation (53) becomes the base area of a caret waverider for $n = m = 1$. Therefore, this term indicates how closely the vehicle corresponds to a caretlike waverider.[2] This leaves Eq. (54) to represent the noncaret waverider base area correction.

The volume V of the variable wedge angle waverider is found from integrating the local base area $S_b(x)$, i.e., replace ℓ with x in Eq. (52), down the length, x, of the vehicle where the solution follows directly as a function of S_b as shown by

$$V = S_b[\ell/(n+2)] \quad (55)$$

The equation for volume is the same regardless of whether the vehicle has a concave or convex lower surface.

Surface area calculation for the variable wedge-angle-derived parametric vehicle requires a simple numerical integration of Eq. (11) for the wetted freestream surface area and the following equation for the wetted compression surface area:

$$S_{wc} = 2\int_0^{\ell}\int_{x\tan\theta}^{x\tan\delta}\sqrt{1 + C^2m^2(z - x\tan\theta)^{2m-2}}\,dz\,dx \quad (56)$$

This results in the total wetted surface area of the vehicle equal to $S_w = S_{w\infty} + S_{wc}$.

Aerodynamic Performance

Lift and Wave Drag

For the purposes of this analysis, even with a curved shock, the flow over the waverider is again assumed to be two dimensional with streamlines flowing straight back over a series of wedges. Because these vehicles do not have uniform spanwise surface angles, the flowfield is solved at each local spanwise angle resulting in what has been termed the variable-wedge-angle (VW) flowfield. Local spanwise angles ϕ_{local} for either the concave or convex vehicles are solved from

$$\phi_{\text{local}} = \tan^{-1}[\Delta z/\xi(y)] \tag{57}$$

where the local vehicle base height Δz is given by

$$\Delta z = \ell[(2y/w)^{1/m}(\tan\delta - \tan\theta) + \tan\theta - (2y/w)^{1/n}\tan\delta] \tag{58}$$

and $\xi(y)$ is solved using Eq. (28). The variations in the local angle across the half-span of the vehicle, the associated compression surface shock pressure ratio, and the exit plane shock profile are shown in Figs. 8 and 9 for the concave and convex vehicles, respectively, where

$$z_{\text{shock,local}} = \xi(y)\tan\beta_{\text{local}} + (2y/w)^{1/n}\ell\tan\delta \tag{59}$$

Following the same format as the constant-wedge-angle waveriders, this method can also easily account for variable angles of attack by using the parameter σ defined for Eqs. (18) and (19). Use of this parameter results in the following lift and wave drag equations by integration of pressure forces at each spanwise location:

$$L = 2\int_0^{A\ell^n} \{\xi(y)[P_l - P_u]\cos|\alpha| + \Delta z(-1)^{\sigma}[P_b - P_l]\sin|\alpha|\}\,dy \tag{60}$$

$$D_w = 2\int_0^{A\ell^n} \{\xi(y)(-1)^{\sigma}[P_l - P_u]\sin|\alpha| + \Delta z[P_l - P_b]\cos|\alpha|\}\,dy \tag{61}$$

where P_u, P_l, and P_b indicate the pressures for the upper, lower, and base surfaces, respectively. These pressures are solved using either the oblique shock or Prandtl–Meyer relations. A vehicle-averaged wedge angle is given by

$$\phi_{\text{av}} = \frac{2\int_0^{A\ell^n}\phi_{\text{local}}\,dy}{w} \tag{62}$$

which is useful as a comparison to θ for the constant-wedge-angle geometries.

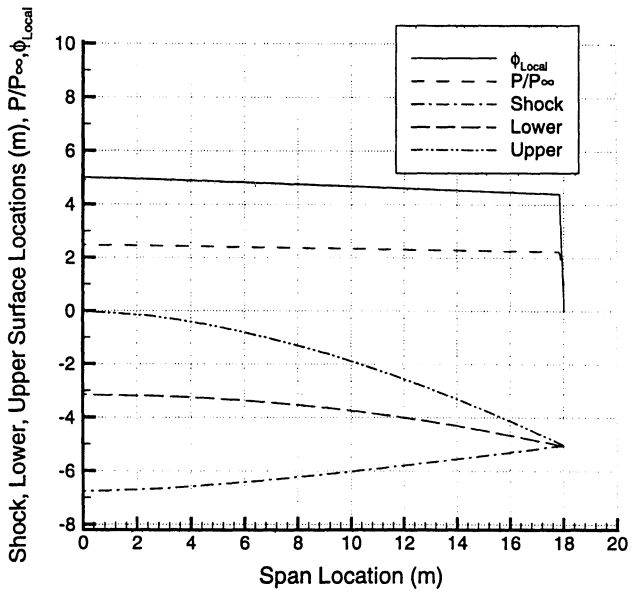

Fig. 8 Variable-wedge-angle concave waverider base plane geometry and shock profiles.

Table 3 Variable-wedge-angle model validation with MAXWARP viscous optimized conical waverider

Variables	MAXWARP	VW	% Diff.
V, m^3	2742	2987	8.94
S_w, m^2	3151	3167	0.51
S_p, m^2	1545	1559	0.91
S_b, m^2	115	121	5.68
η_{S_p}	0.1268	0.1330	4.89
η_{S_w}	0.0622	0.0655	5.35
η_{S_s}	0.3007	0.3168	5.37
η_{V_s}	0.1647	0.1783	8.26
L/D	7.88	8.13	4.19
L ($\times 10^6$ N)	7.782	8.113	−0.28
D_w ($\times 10^6$ N)	0.635	0.633	3.61
D_v ($\times 10^6$ N)	0.352	0.365	3.16

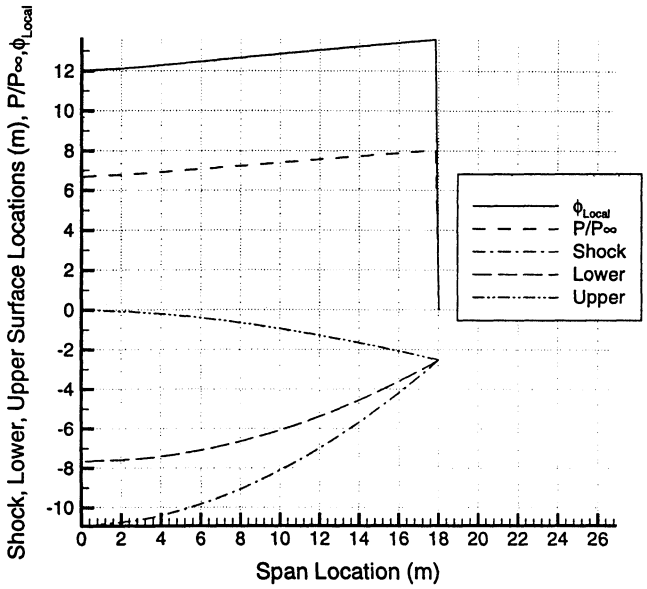

Fig. 9 Variable-wedge-angle convex waverider base plane geometry and shock profiles.

Viscous Drag

The skin friction for both laminar and turbulent flows are solved in the same manner as shown for the constant-wedge-angle waveriders. Because the upper surface is at a constant angle relative to freestream, it can be solved in the same way as the planar shock waverider. When solving for the lower surface, the bounds of integration use the spanwise angle ϕ_{local} instead of the vehicle centerline wedge angle θ. This results in the total vehicle viscous drag equation

$$D_v = G_{1,u}w\ell^{G_2}F(n) + \int_0^{A\ell^n}\int_0^{\xi_u(y)/\phi_{\text{local}}(y)} \frac{1.6G_{1,l}[\phi_{\text{local}}(y)]}{x^{1-G_2}}\,dx\,dy \tag{63}$$

where G_1, G_2, and $F(n)$ are the viscous drag parameters shown in Table 1.

The implicit drawbacks to this method are as follows: 1) The model is assumed to be a true aerodynamic shape with no losses due to engine–airframe integration (a reasonable approximation for a rocket application); 2) all values of lift and drag assume shock attachment to the leading edge, i.e., no pressure leakage, which is

Table 4 Variable-wedge-angle model off-design Mach number and angle-of-attack validation with Euler CFD calculations of an optimized osculating-cone waverider

		Lift ($\times 10^5$ N)			Wave drag ($\times 10^5$ N)			L/D_w		
M_∞	α, deg	OC	*VW*	% Error	OC	*VW*	% Error	OC	*VW*	% Error
4	0	14.62	15.01	2.67	3.632	3.716	2.30	4.03	4.04	0.36
6	0	11.08	11.15	0.68	2.145	2.162	0.77	5.16	5.16	−0.09
8	0	9.356	9.377	0.22	1.566	1.570	0.28	5.97	5.97	−0.06
10	0	8.379	8.441	0.73	1.276	1.286	0.74	6.57	6.57	0.00
10	−6	−6.194	−6.945	12.12	1.013	1.095	8.10	−6.11	−6.34	3.72
10	−4	−1.443	−1.813	25.65	0.675	0.705	4.39	−2.14	−2.57	20.36
10	−2	3.344	3.239	−3.13	0.757	0.767	1.27	4.42	4.22	−4.35
10	0	8.379	8.441	0.73	1.276	1.286	0.74	6.57	6.57	0.00
10	2	13.84	14.01	1.20	2.274	2.294	0.86	6.09	6.11	0.34
10	4	19.87	20.10	1.20	3.813	3.849	0.95	5.21	5.22	0.25
10	6	26.53	26.84	1.16	5.968	6.027	0.99	4.45	4.45	0.17

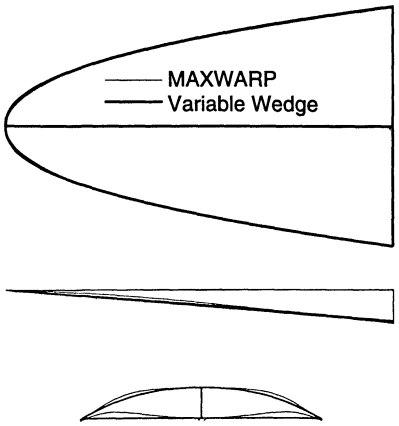

Fig. 10 Variable-wedge-angle model geometry comparison with MAXWARP conical waverider.

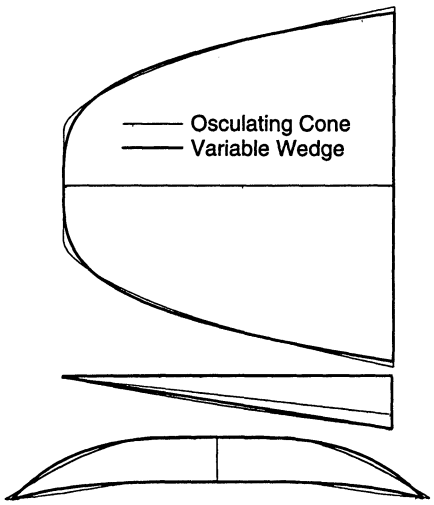

Fig. 11 Variable-wedge-angle model geometry comparison with osculating-cone waverider.

not true for all sets of parameters in this method; 3) centrifugal lift has been neglected; 4) transverse flow is assumed to be zero; 5) the wall temperature is assumed to be constant; and 6) viscous drag errors increase for more cylindrical vehicles.

Validation Models

MAXWARP Conically Derived Waveriders

Using the MAXWARP[6] optimization code, a suitable conically derived waverider comparison model was generated (a Mach 8 cruiser optimized for maximum L/D).

The planform leading-edge equation ($y = Ax^n$) was curve fit to the MAXWARP vehicle resulting in values of $n = 0.440$ and $m = 0.050$ for the power law exponents. The resulting variable wedge-angle geometry match is shown in Fig. 10. As Fig. 10 shows, the values of ℓ, w, h, θ, and δ (60 m, 37.43 m, 4.98 m, 4.532 deg, and 4.740 deg, respectively) were all held constant between the two vehicles. The freestream Mach number and dynamic pressure (determined by MAXWARP optimization) were also held constant at 8 and 1.84 atm, respectively.

Specifications are shown in Table 3 for both the MAXWARP vehicle and the resulting variable wedge *VW* approximation. The variable wedge vehicle has a 8.9% larger volume and 5.7% larger base area. The outcome was a model that had a 3.2% larger L/D, 4.2% more lift, 0.3% less wave drag, and 3.2% more viscous drag than the MAXWARP vehicle. Therefore, it is clearly shown that the variable wedge model is able to simply and analytically solve for the same characteristics that take orders of magnitude more time to solve using the conical method. Also, it is important to note that the variable wedge model produces the same result as the conical method while producing a geometry with higher efficiencies and without the unrealistically thin rearward leading edges.

Osculating Cone-Derived Waveriders

The method of osculating cones[7] (OC) is an infinite-degree-of-freedom tool used for inverse waverider design. Using models generated by Takashima[8] with this method, a comparison was made to validate off-design performance for different Mach numbers and angles of attack. Takashima validated the method of osculating cones using an inviscid computational fluid dynamics (CFD) calculation of the optimized Mach 10 vehicle shown in Fig. 11. The vehicle approximation was made using the variable-wedge-angle method by curve fitting ($y = Ax^n$) to the planform surface of the osculating cone-generated waverider. The vehicle approximation is fairly close to the desired shape with only slight differences in the resulting geometries. They were matched to have equal length, width, height, and centerline and leading edge angles of 22.12 m, 24.16 m, 3.50 m, 6.56 deg, and 9.00 deg, respectively.

The comparisons to the off-design CFD calculations are shown for Mach numbers between 4 and 10 and angles of attack between −6 and 6 deg are shown in Table 4. Data are given for the lift, wave drag, and L/D_w for the CFD osculating cone and analytical variable-wedge-angle calculations. All results agree with the CFD validation numbers other than for the $\alpha = -4$ deg cases. The error for these cases is 20% because this angle is close to the vehicle's zero lift angle of about 3.3 deg, i.e., low magnitude of lift results in a large error with small departures from the solution. Coincidentally, the variable-wedge-angle and osculating-cone methods had the same magnitude of errors (maximum difference was at $\alpha = -4$ deg and was 2.4%) in comparison to the Euler CFD calculation, although the variable-wedge-angle method is orders of magnitude faster to calculate. This makes the variable-wedge-angle method an extremely powerful tool for parametric studies of hypersonic waveriders.

Conclusions

Use of a parametric vehicle will allow for quick analytical studies to help determine a first-order approximation for a desirable vehicle configuration. Toward this goal, a power law derived vehicle model

has been developed that can generate planar-shock geometries (four variable parameters) or waveriders with three-dimensional shocks (six variable parameters). Because of the three-dimensional nature of the model, a variable-wedge-angle analysis has been developed that can be fit to more realistic configurations. This method has been validated using both conically and osculating-cone-derived waveriders. The variable-wedge-angle method has been shown to have the same accuracy as both the conical and the osculating-cone methods for optimized waverider configurations (including viscous effects, as well as off-design Mach numbers and angles of attack), thereby making the variable-wedge-angle method extremely powerful for parametric studies of hypersonic waveriders. Also, because the planar shock model is contained as a subset of the variable-wedge-angle model, i.e., fewer parameters, it allows for even greater insight into the characteristics of these type of vehicles.

Acknowledgments

This research was supported by the Center for Hypersonic Education and Research at the University of Maryland under Technical Monitor Isaiah Blankson of NASA (NASA Grant NAGw 11796), as well as by the Boeing Space Transportation Concepts and Analysis Business Development Division under Technical Monitor Dana Andrews (Boeing Contract JQ4085), whose support is greatly appreciated.

References

[1]Nonweiler, T. R. F., "Aerodynamic Problems of Manned Space Vehicles," *Journal of the Royal Aeronautical Society*, Vol. 63, Sept. 1959, pp. 521–528.

[2]Rasmussen, M., *Hypersonic Flow*, 1st ed., Wiley-Interscience, New York, 1994, pp. 100–108.

[3]Gillum, M. J., and Lewis, M. J., "Experimental Results on a Mach 14 Waverider with Blunt Leading Edges," *Journal of Aircraft*, Vol. 34, No. 3, 1997, pp. 296–303.

[4]Takashima, N., and Lewis, M. J., "Navier–Stokes Computation of a Viscous Optimized Waverider," AIAA Paper 92-0305, Jan. 1992.

[5]White, F. M., *Viscous Fluid Flow*, 1st ed., McGraw–Hill, New York, 1974, pp. 28, 589–592.

[6]Corda, S., and Anderson, J. D., "Viscous Optimized Hypersonic Waveriders Designed from Axisymmetric Flowfields," AIAA Paper 88-0369, Jan. 1988.

[7]Center, K. B., Sobieczky, H., and Dougherty, F. C., "Interactive Design of Hypersonic Waverider Geometries," AIAA Paper 91-1697, June 1991.

[8]Takashima, N., "Optimization of Waverider Based Hypersonic Vehicle Designs," Ph.D. Dissertation, Dept. of Aerospace Engineering, Univ. of Maryland, College Park, MD, May 1997.

R. M. Cummings
Associate Editor